SUB | NIEDERSÄCHSISCHE STAATS- UND UNIVERSITÄTSBIBLIOTHEK GÖTTINGEN

Werk

Jahr: 1977
Kollektion: fid.geo
Signatur: 8 Z NAT 2148:
Digitalisiert: Niedersächsische Staats- und Universitätsbibliothek Göttingen
Werk Id: PPN1015067948_0043
PURL: http://resolver.sub.uni-goettingen.de/purl?PPN1015067948_0043

LOG Id: LOG_0048
LOG Titel: Finite difference calculation of stress relaxation earthquake models
LOG Typ: article

Übergeordnetes Werk

Werk Id: PPN1015067948
PURL: http://resolver.sub.uni-goettingen.de/purl?PPN1015067948
OPAC: http://opac.sub.uni-goettingen.de/DB=1/PPN?PPN=1015067948

Terms and Conditions

The Goettingen State and University Library provides access to digitized documents strictly for noncommercial educational, research and private purposes and makes no warranty with regard to their use for other purposes. Some of our collections are protected by copyright. Publication and/or broadcast in any form (including electronic) requires prior written permission from the Goettingen State- and University Library.
Each copy of any part of this document must contain there Terms and Conditions. With the usage of the library's online system to access or download a digitized document you accept the Terms and Conditions.
Reproductions of material on the web site may not be made for or donated to other repositories, nor may be further reproduced without written permission from the Goettingen State- and University Library.

For reproduction requests and permissions, please contact us. If citing materials, please give proper attribution of the source.

Contact

Niedersächsische Staats- und Universitätsbibliothek Göttingen
Georg-August-Universität Göttingen
Platz der Göttinger Sieben 1
37073 Göttingen
Germany
Email: gdz@sub.uni-goettingen.de

J. Geophys. 43, 311–327, 1977

Journal of Geophysics

Finite Difference Calculation of Stress Relaxation Earthquake Models*

H. Stöckl

Geophysikalisches Institut der Universität Karlsruhe,
Hertzstr. 16, D-7500 Karlsruhe, Federal Republic of Germany

Abstract. Two types of earthquake sources corresponding to the longitudinal and the transverse shear crack are considered. First, 2 standard models are treated which are characterized by homogeneous prestress, plane or anti-plane strain, symmetrical crack propagation at a constant fracture velocity up to a given final crack length, and 100 % stress drop. The displacement time functions can be interpreted in terms of various types of waves originating both from the initiation and the termination of the fracture. Next, fracture experiments with nonhomogeneous prestress are simulated. Finally it is shown for the longitudinal shear crack how the fracture velocity v_r can be calculated if the fracture energy is specified. The crack starts to grow from a critical initial length at $v_r \approx 0$. Crack growth accelerates rapidly, and when the length has doubled, v_r reaches 54 % of the shear wave velocity, which turns out to be the terminal velocity in this case. The elastodynamic problems are solved with a modification of a finite difference method published by Alterman and Rotenberg.

Key words: Earthquake models – Stress relaxation source – Finite difference method.

1. Introduction

Until recently, earthquake sources were mainly modelled as dislocations or equivalent forces (Burridge and Knopoff, 1964). In the dislocation models the displacement time function is assumed on a fault plane and is calculated in the surrounding elastic medium with a representation theorem (Haskell, 1969). The motion in the earthquake focus, however, results from a relaxation of an initial stress state: In a certain region, usually visualized as a plane, the physical conditions determining the stress change, and the prestress is no longer in

* Contribution no. 145, Geophysical Institute, University of Karlsruhe

equilibrium. According to the elastodynamic equation of motion, the material around the fault plane will move and radiate seismic waves. The stress in the "fractured" region, in turn, may depend on the particle velocity, the temperature, and various rock properties. The fault plane will grow according to some "fracture" criterion until an arrest criterion is met. Finally a new equilibrium is established.

Earthquake source models constructed according to these ideas will have some obvious advantages (see Archambeau, 1968): Energy, linear and angular momentum are conserved as required for a spontaneous source. The motion in the focal region is calculated and has not to be assumed beforehand. If prestress and material behaviour are given, the model predicts the complete time history of the focal event. At present, detailed and reliable laboratory or field data about material behaviour in the focal region are not available. Despite this, it seems more plausible to assume physically reasonable conditions concerning the stress on the fault plane than to guess the time function of the displacement.

Further references concerning the work done on stress relaxation models both analytically and numerically can be found in Richards (1976), Madariaga (1976), Andrews (1976) and Stöckl (1976). In the present paper, the elastodynamic problems are solved with a modification of a finite difference method due to Alterman and Rotenberg (1969). This powerful tool solves many problems too difficult for an analytic treatment. The method is applied to some simple stress relaxation earthquake sources, to fracture propagation with specified fracture energy, and to the simulation of fracture experiments.

2. Standard Models of Stress Relaxation Earthquake Sources

Since the focal process is related to fracture, the concepts of fracture mechanics should be useful in the discussion of earthquake sources. There are three basic types of cracks, the so-called fracture modes (Fig. 1). The arrows at the outer boundaries represent the applied stress, the arrows at the crack surfaces represent the resulting displacement.

In analogy to these fracture modes we define three standard models SI, SII, SIII as follows. Consider a block of homogeneous, isotropic, brittle, elastic material. Let x, y, z be Cartesian coordinates, t the time, and $\mathbf{s}(x, y, z, t)$ the displacement vector with the components u, v, w. The initial conditions are

$$\partial \mathbf{s}(x, y, z, 0)/\partial t = \mathbf{0}, \tag{1}$$

and for the standard model

$$\text{SI:} \quad \sigma_{yy}(x, y, z, 0) = \sigma^0_{yy} = \text{const} \tag{2a}$$

$$\text{SII:} \quad \tau_{xy}(x, y, z, 0) = \tau^0_{xy} = \text{const} \tag{2b}$$

$$\text{SIII:} \quad \tau_{yz}(x, y, z, 0) = \tau^0_{yz} = \text{const}, \tag{2c}$$

where σ_{yy}, τ_{xy} and τ_{yz} are stress components.

A state of plane strain is assumed for SI and SII:

$$w = 0, \quad \partial u/\partial z = \partial v/\partial z = 0, \tag{3}$$

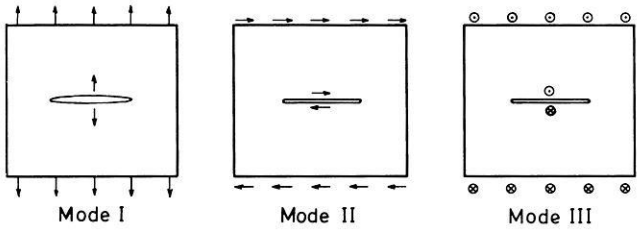

Fig. 1. Schematic representation of the applied stress and the crack wall displacement for three basic types of fractures. Mode I: tensile crack, Mode II: transverse shear crack, Mode III: longitudal shear crack

while for SIII we have a state of antiplane strain (or out-of-plane shear):

$$u=v=0, \quad \partial w/\partial z=0. \tag{4}$$

We assume then that a crack is initiated at $x=y=0$, $t=0$ and propagates along the x-axis in both directions at a constant speed v_r up to its final length $2L_f$, where it stops suddenly. The crack walls are free surfaces, that is

$$\sigma_{yy}=\tau_{xy}=\tau_{yz}=0 \quad \text{for } y=0, x\leqq L(t), \tag{5}$$

where

$$L(t)=v_r t \qquad \text{for } t\leqq L_f/v_r,$$

$$L(t)=L_f \qquad \text{for } t\geqq L_f/v_r.$$

These standard models are the simplest conceivable stress relaxation models. They are not supposed to be realistic models of the focal process, they may, however, serve as a standard for comparison with more realistic models. Despite this, some essential features of earthquakes are correctly modelled, as we shall see later. Model SI, which has been studied by Stöckl and Auer (1976) and Stöckl (1976b), will not be treated here. It is more important in engineering rather than in focal mechanism studies.

3. Method of Computation

3.1. Discretization of the Equation of Motion

The computational method was adopted from the publications of Alterman and her co-workers. There are some deviations from their procedure, which will be indicated.

The equation of motion is

$$\rho(\partial^2\mathbf{s}/\partial t^2)=(\lambda+2\mu)\,\text{grad div}\,\mathbf{s}-\mu\,\text{curl curl}\,\mathbf{s}, \tag{6}$$

where λ, μ are Lamé's constants and ρ is the density. In two dimensions under

plane strain or antiplane strain conditions, Equation (6) can be written in the following form:

$$\partial^2 u/\partial t^2 = \alpha^2(\partial^2 u/\partial x^2) + (\alpha^2 - \beta^2)(\partial^2 v/\partial x\,\partial y) + \beta^2(\partial^2 u/\partial y^2)$$

$$\partial^2 v/\partial t^2 = \alpha^2(\partial^2 v/\partial y^2) + (\alpha^2 - \beta^2)(\partial^2 u/\partial x\,\partial y) + \beta^2(\partial^2 v/\partial x^2) \tag{7a}$$

$$\partial^2 w/\partial t^2 = \beta^2(\partial^2 w/\partial x^2 + \partial^2 w/\partial y^2), \tag{7b}$$

with $\alpha^2 = (\lambda + 2\mu)/\rho$, $\beta^2 = \mu/\rho$. α and β are the compressional and shear wave velocity, respectively.

In the finite difference approximation the partial derivatives of Equations (7a, b) at $t = n \cdot \Delta t$, $x = i \cdot s$, $y = j \cdot s$ are replaced by centred differences in the following way (see Fig. 2a):

$$(\partial^2 u/\partial t^2)^n_{i,j} = (u^{n+1}_{i,j} - 2u^n_{i,j} + u^{n-1}_{i,j})/\Delta t^2$$

$$(\partial^2 u/\partial x^2)^n_{i,j} = (u^n_{i+1,j} - 2u^n_{i,j} + u^n_{i-1,j})/s^2$$

$$(\partial^2 u/\partial x\,\partial y)^n_{i,j} = (u^n_{i+1,j+1} - u^n_{i-1,j-1} - u^n_{i+1,j-1} + u^n_{i-1,j-1})/4s^2 \quad \text{etc.}, \tag{8}$$

where we write, for example, $u(x, y, t) = u^n_{i,j}$ as a short hand notation.

We now choose $\lambda = \mu$, which implies $\alpha^2 = 3\beta^2$ and $\Delta t = s/2\beta$ in the plane strain case, Equation (7a), and $\Delta t = s/\sqrt{2}\,\beta$ in the antiplane strain case, Equation (7b). Solving for $u^{n+1}_{i,j}$, $v^{n+1}_{i,j}$, $w^{n+1}_{i,j}$ we obtain from Equations (7a, b) and (8) the following explicit recursive formulas:

$$\begin{aligned} u^{n+1}_{i,j} = {} & -u^{n-1}_{i,j} + \tfrac{1}{4}[3(u^n_{i+1,j} + u^n_{i-1,j}) + u^n_{i,j+1} + u^n_{i,j-1} \\ & + \tfrac{1}{2}(v^n_{i+1,j+1} - v^n_{i-1,j+1} - v^n_{i+1,j-1} + v^n_{i-1,j-1})] \\ v^{n+1}_{i,j} = {} & -v^{n-1}_{i,j} + \tfrac{1}{4}[3(v^n_{i,j+1} + v^n_{i,j-1}) + v^n_{i+1,j} + v^n_{i-1,j} \\ & + \tfrac{1}{2}(u^n_{i+1,j+1} - u^n_{i-1,j+1} - u^n_{i+1,j-1} + u^n_{i-1,j-1})] \end{aligned} \tag{9a}$$

$$w^{n+1}_{i,j} = -w^{n-1}_{i,j} + \tfrac{1}{2}(w^n_{i+1,j} + w^n_{i-1,j} + w^n_{i,j+1} + w^n_{i,j-1}). \tag{9b}$$

The chosen time steps are critical values; larger time steps would lead to an unstable scheme (Alterman and Loewenthal, 1970). The critical values are preferred in this work, because they give the most satisfactory result and because they lead to simpler recursive formulas. Alterman and her co-workers used slightly subcritical time steps.

3.2. Discretization of the Boundary Conditions

Since the problems are symmetric with respect to the x- and y-axis, one only needs to calculate the quarter plane $x \geqq 0$, $y \geqq 0$. Figure 2 shows 3 possibilities of arranging the grid with respect to the crack. The boundary- and symmetry conditions are satisfied with fictitious grid points (symbols x in Fig. 2). We shall discuss here only the arrangement of Figure 2b. For convenience we define here $y = j \cdot s - s/2$ instead of $y = j \cdot s$. Along the y-axis and along the x-axis beyond the

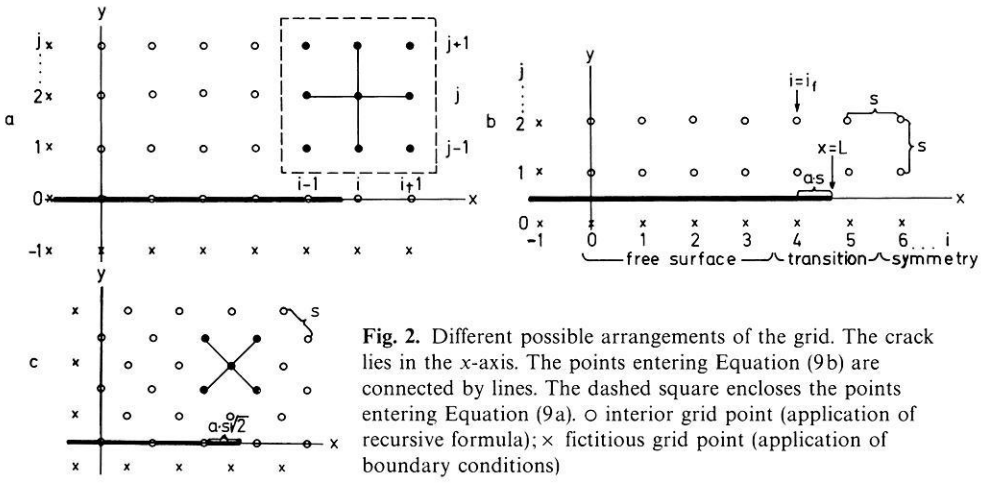

Fig. 2. Different possible arrangements of the grid. The crack lies in the x-axis. The points entering Equation (9b) are connected by lines. The dashed square encloses the points entering Equation (9a). o interior grid point (application of recursive formula); × fictitious grid point (application of boundary conditions)

crack tip the displacement of the fictitious grid points follow from symmetry (the superscript n is dropped):

$$\text{SII}\begin{cases} u_{-1,j} = u_{1,j}, & v_{-1,j} = -v_{1,j} \\ u_{i,1} = -u_{i,0}, & v_{i,1} = v_{1,0} \quad \text{for } i > i_f + 1 \end{cases} \tag{10a, 10b}$$

$$\text{SIII}\begin{cases} w_{-1,j} = w_{1,j} \\ w_{i,1} = -w_{i,0} \quad \text{for } i > i_f + 1. \end{cases} \tag{10c, 10d}$$

Along the crack surfaces, the boundary conditions, Equation (5), can be written for $\lambda = \mu$ as follows:

$$\partial u/\partial x + 3\,\partial v/\partial y = 0 \quad (\sigma_{yy} = 0) \tag{11a}$$

$$\partial u/\partial y + \partial v/\partial x = 0 \quad (\tau_{xy} = 0) \tag{11b}$$

$$\partial w/\partial y = 0 \quad (\tau_{yz} = 0). \tag{11c}$$

The derivatives with respect to y may be approximated by centred differences with respect to the free surface $y = 0$, such as

$$(\partial w/\partial y)_{i,\frac{1}{2}} = (w_{i,1} - w_{i,0})/s. \tag{12}$$

Equations (11c) and (12) lead to

$$w_{i,0} = w_{i,1} \quad \text{for } i < i_f. \tag{13}$$

If the fracturing grid point is released suddenly at the moment when the crack passes, the energy stored at the crack tip is converted into large oscillations with a period of a few time steps. In the physical analogue the individual atoms oscillate when the bonds between them are broken. These oscillations may be regarded as heat. In the numerical simulation the oscillations disturb the results. They can be reduced very much, if, for example, the grid point $i_f + 1$ is

released gradually while the crack runs from $x=i_f \cdot s$ to $x=(i_f+2)s$ (Fig. 2). In the transition zone work is done against the forces exerted by the fictitious grid points, which simulates the fracture energy, because both the stress and the displacement at $y=0$ are nonzero ($\tau_{yz}(x,0)$ and $w(x,0)\approx\frac{1}{2}(w_{i,0}+w_{i,1})$ in SIII).

We obtain a reasonable transition, if we take a weighted mean of Equation (10d), which holds for the infractured state, and Equation (13), which holds for the stress free state, in the following way:

$$\begin{aligned} w_{i_f,0} &= w_{i_f,1} \cdot a \\ w_{i_f+1,0} &= w_{i_f+1,1} \cdot (a-1), \end{aligned} \tag{14}$$

where $a=L(t)/s-i_f$ (see Fig. 2).

In the case of the models SI and SII two possibilities of representing the boundary conditions (Eq. (11a, b)) were examined:

i) The derivatives with respect to y are treated in the same fashion as Equation (12), whereas for the derivatives with respect to x the mean of the centred differences at the grid lines $j=0$ and $j=1$ is taken, for example

$$(\partial u/\partial x)_{i,\frac{1}{2}}=(u_{1,i+1}-u_{1,i-1}+u_{0,i+1}-u_{0,i-1})/4s. \tag{15}$$

This leads to a system of equations for the unknown $u_{0,i}$, $v_{0,i}$. The transition zone can be handled in a similar fashion as in Equation (14). This possibility is described in more detail in Stöckl and Auer (1976) and Stöckl (1976).

ii) The derivatives are calculated at the centre of the mesh $x=(i+\frac{1}{2})s$, $y=0$. They are approximated by the following average differences:

$$\begin{aligned} (\partial u/\partial x)_{i+\frac{1}{2},\frac{1}{2}} &= (u_{i+1,1}-u_{i,1}+u_{i+1,0}-u_{i,0})/2s \\ (\partial v/\partial y)_{i+\frac{1}{2},\frac{1}{2}} &= (v_{i,1}-v_{i,0}+v_{i+1,1}-v_{i+1,0})/2s. \end{aligned} \tag{16}$$

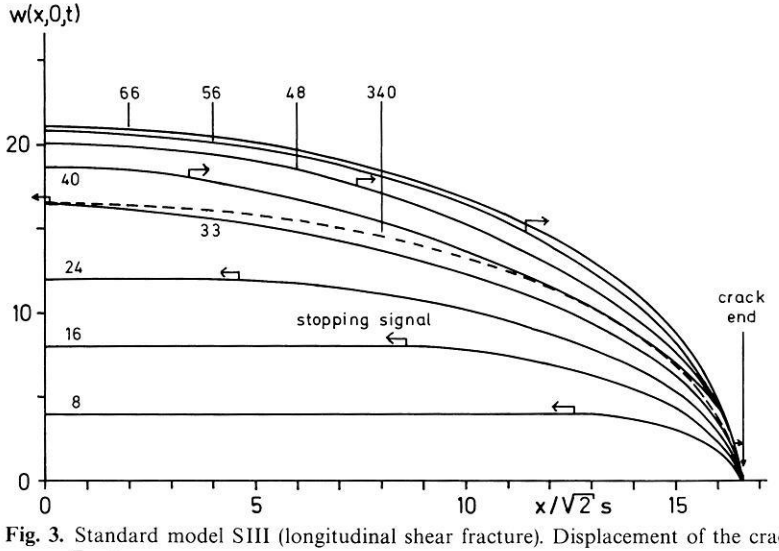

Fig. 3. Standard model SIII (longitudinal shear fracture). Displacement of the crack walls $w(x,0,t)$ (unit $\sqrt{2}\,s\,\tau^0_{yz}/\mu$). Fracture velocity: $v_r\to\infty$. Parameter: time step n

This approach leads again to a system of equations for the unknowns $v_{i,0}$, $u_{i,0}$ with a tridiagonal matrix. Assuming that the stress at $x=(i+\frac{1}{2})s$ is $(1-a)$ times the stress which would arise there if $a=0$, one obtains a suitable transition zone. More details about this procedure are found in Stöckl (1976).

Both approaches i) and ii) are equivalent in accuracy to centred differences, therefore the solution has a truncation error of the second order in s/L in the static and low frequency part of the solution.

Alterman and her co-workers put a grid line in the free surface (Fig. 2a). One might try to approximate the normal derivatives by centred differences, writing, for example, $(\partial w/\partial y)_{i,0}=(w_{i,1}-w_{i,-1})/2s$ instead of Equation (12), which is a centred difference for the arrangement of Figure 2b. However, the resulting scheme is unstable, and this is also true for the plane strain case (Alterman et al., 1971). They obtained a stable scheme with one-sided differences, but the solution had a truncation error of first order in s/L only. Recently, however, Ilan et al. (1975) developed an improved representation with a truncation error of second order.

4. Near Field Displacement for the Standard Models

4.1. Standard Model SIII

In the first example the crack appears instantaneously, that is, $v_r\to\infty$. For some reasons discussed later the grid was arranged as in Figure 2c.

Figure 3 shows the displacement of the crack surfaces. The results are interpreted as follows: The stress drop from τ^0_{yz} to zero propagates in the y-direction at the shear wave velocity β. Behind the wave front, which is parallel to the x-axis, the material moves at the velocity $\partial w/\partial t=\beta\tau^0_{yz}/\mu$. The crack ends radiate cylindrical wave fronts, the stopping signals, which lower the constant particle velocity just mentioned. They appear as slight kinks in the curves of Figure 3. Arrows drawn at the theoretically expected places indicate their propagation direction.

At the time $t=L_f/\beta$ ($n\approx 33$) the signal reaches the middle of the crack. The displacement at this point is $w(0,0,L_f/\beta)=L_f\tau^0_{yz}/\mu$, which happens to be equal to the static value. Since the crack walls still move, they overshoot the equilibrium. After this time the stopping signal of the other crack tip enters the figure and reaches the drawn tip at $t=2L_f/\beta$ ($n\approx 66$). In this moment, as it turns out, the crack walls attain a maximum displacement, which exceeds the static value by 27 %. $w(x,0,2L_f/\beta)$ is elliptical as a function of x. Since equilibrium is not yet established, the crack walls, although momentarily at rest, begin to move backwards and fall 3 % below the static value. The stopping signals running parallel to the crack are partly diffracted backwards, but most of the energy is radiated away. While the diffraction repeats again and again, the motion becomes damped oscillatory and the displacement around the crack approaches the static solution. The dashed curve ($n=340$) differs from the final value by about 1/1000. It agrees with the analytic solution

$$w(x,0,\infty)=L_f(\tau^0_{yz}/\mu)(1-x^2/L_f^2)^{1/2}$$

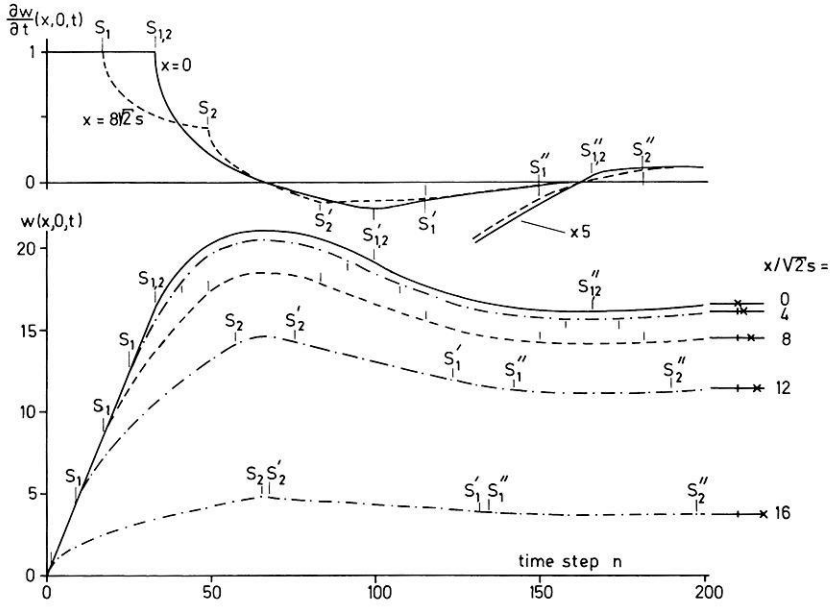

Fig. 4. Standard model SIII (the same example as in Fig. 3). Displacement of the crack walls $w(x, 0, t)$ and velocity $\partial w(x, 0, t)/\partial t$ (unit $\beta \tau^0_{yz}/\mu$). Parameter: $x/\sqrt{2}s$. S_1, S_2: Stopping signals from the near and far crack end. S'_1, S'_2, S''_1, S''_2: Stopping signals diffracted once and twice

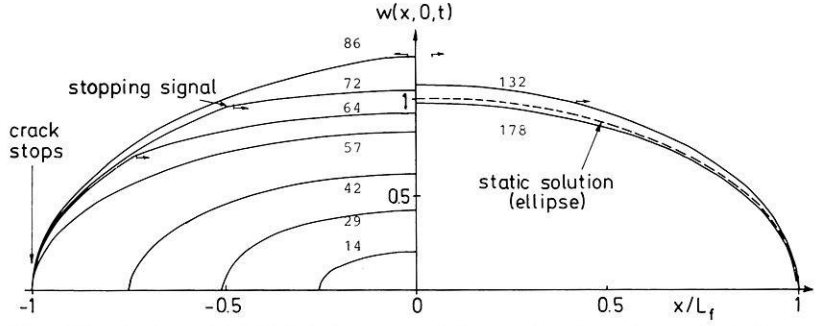

Fig. 5. Standard model SIII. Displacement of the crack walls (unit: $L_f \tau^0_{yz}/\mu$). Fracture velocity $v_r = 0.5\beta$. Parameter: time step n

within drawing accuracy. Assuming that the finite difference solution is equal to the analytic solution for $w(0, 0, \infty)$ one obtains an effective crack length, which is $L_f = 16.6\sqrt{2}\,s$ in this example.

Figure 4 shows the displacement of the crack walls as a function of time. The theoretical arrival times of the different direct and diffracted stopping signals are marked. On the displacement curves the signals are hardly seen. Therefore, the particle velocity $\partial w/\partial t$ of two of the curves is drawn above them. The direct stopping signals and the stopping signals diffracted once appear as clear kinks. Magnified fivefold, the stopping signals diffracted twice are also evident.

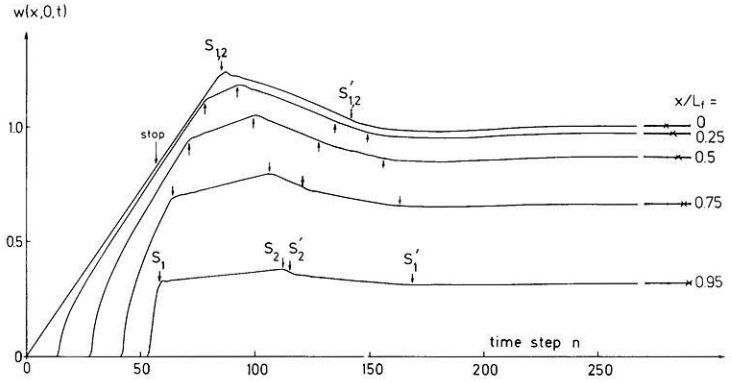

Fig. 6. Standard model SIII (the same example as in Fig. 5). Displacement of the crack walls $w(x, 0, t)$. Parameter: x/L_f

In the next example the fracture velocity is $v_r = 0.5\,\beta$. The grid was arranged as in Figure 2b. Figure 5 shows the displacement of the crack walls in a similar fashion as Figure 3. The crack length is $L_f = 20 \cdot s$. Up to $n = 86$ the left half of the crack is plotted, after this the right half. Erdogan (1968) gives an analytic solution valid for the time before the crack stops. For $v_r \leqq \beta$ the displacement of the crack walls is elliptical as a function of x. The finite difference solution agrees well with this result except at the crack tips, where the curves are smoothed due to the transition zone. When the crack stops, stopping signals are produced which behave similarly to the example described before.

In Figure 6 the displacement of the crack walls is plotted as a function of time. Before the first stopping signal arrives, the crack centre moves at a constant velocity, which agrees completely with the analytic value

$$\partial w(0,0,t)/\partial t = v_r(\tau_{yz}^0/\mu)/E((1-v_r^2/\beta^2)^{\frac{1}{2}}) \quad \text{for} \quad v_r \leqq \beta, \tag{17}$$

where $E(x) = \int_0^{\pi/2} (1 - x^2 \sin^2\psi)^{\frac{1}{2}}\, d\psi$ is the complete elliptical integral of the second kind. For $x/L_f > 0$ we obtain hyperbolas approaching asymptotically the straight line, which holds for $x/L_f = 0$. This follows from the fact that the crack wall displacements are elliptical as a function of x. At the apex of the hyperbolas the velocity and the acceleration are singular. In the difference solution the discretization and the transition zone remove the singularity, whereas in nature this is done by the atomic structure and by plastic deformation. The stopping signals are more distinct in this example than in Figure 3, since they are associated with a jump in the particle velocity. The curves have their maximum when the stopping signal arrives from the remote crack end.

4.2. Standard Model SII

Alterman et al. (1971) have already calculated the instantaneously appearing transverse shear crack, that is SII with $v_r \to \infty$. The results presented here agree with their findings, but are interpreted somewhat differently.

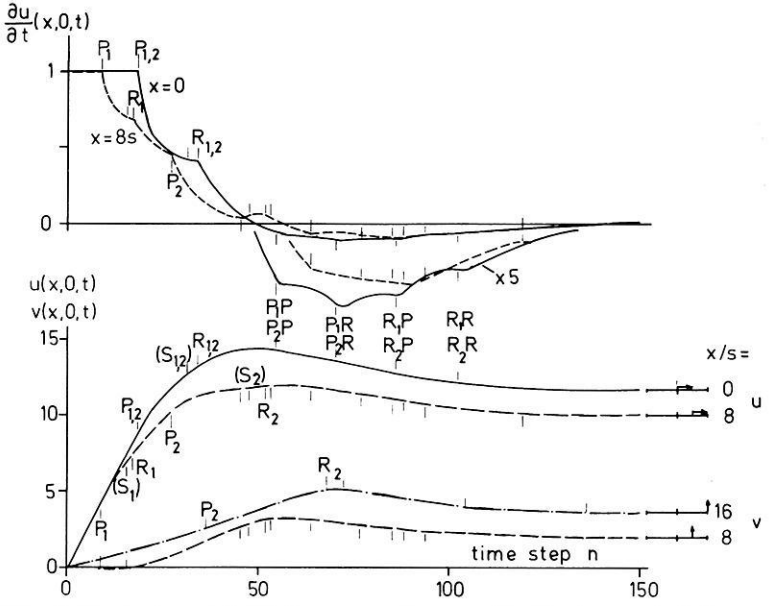

Fig. 7. Standard model SII (transverse shear crack). Displacement of the crack walls $u(x,0,t)$, $v(x,0,t)$ (see sketch on the right side). Unit: $s\tau^0_{xy}/\mu$. Above: velocity $\partial u(x,0,t)/\partial t$ (unit: $\beta\tau^0_{xy}/\mu$). Fracture velocity: $v_r \to \infty$. Parameter: x/s. Not all of the stopping signals are identified

Figure 7 shows the time functions of the displacement components u and v at the crack surface, as indicated by the sketch to the right. Similarly as in Figure 4 the stopping signals show up clearly only in the time derivatives. In the continuous curves, which represent $u(0,0,t)$ and $\partial u(0,0,t)/\partial t$ the first stopping signal travelling at the velocity α arrives at $n \approx 18$. It is labelled P_1, P_2 (1 and 2 refers to the near and far crack end, respectively). No arrival is seen at $n=31$, where a signal travelling at the velocity β is expected (S_1, S_2). According to the travel time, the kink at $n=34$, labelled R_1, R_2 appears to be a Rayleigh wave, travelling at $v_R = 0.92\,\beta$. The stopping signals P and R are diffracted backwards at the other crack end as waves of the same type and as converted waves. These signals are seen after 5 fold magnification. The labels P_1P, P_1R, ... mean signals travelling from the near crack end to the far end at the velocity α and from there to the observation point at the velocity α and v_R respectively.

In the next example the fracture velocity $v_r = 0.3\,\alpha \approx 0.52\,\beta$ was chosen. The component $u(x,0,t)$ has the shape of an ellipse up to $n=60$, when the crack stops (Fig. 8). On this representation the stopping signals are hardly seen. The component $v(x,0,t)$ shows that the crack rotates counterclockwise, whereas the relative displacement of the crack walls is right-handed. As long as the crack runs it remains straight. During the presence of the stopping signals it is distorted, but straightens again in the static case, which is approximately reached at $n=200$.

Figure 9 shows the time function of the displacement. The signals labelled P and S on the component $v(x,0,t)$ are radiated when the crack starts. They

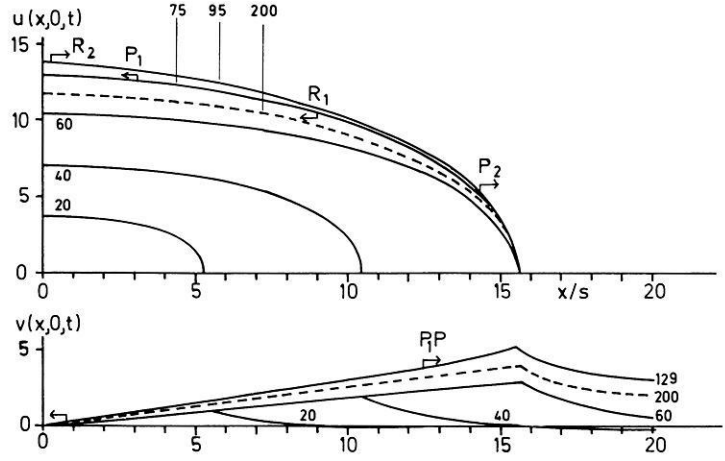

Fig. 8. Standard model SII (transverse shear crack). Displacement of the crack walls $u(x, 0, t)$, $v(x, 0, t)$ (unit: $s\tau^0_{xy}/\mu$). Fracture velocity $v_r = 0.3\,\alpha$. Parameter: time step n

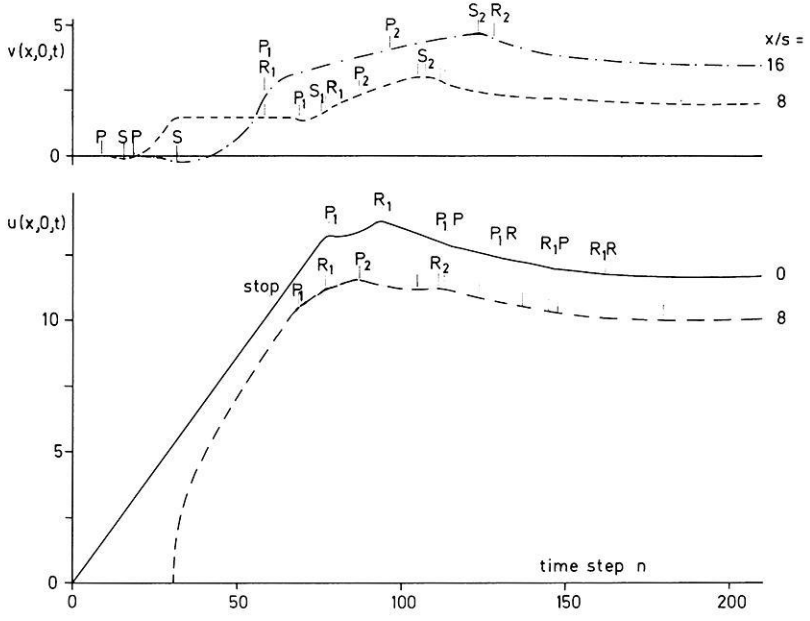

Fig. 9. Standard model SII (the same example as in Fig. 8). Displacement of the crack walls $u(x, 0, t)$, $v(x, 0, t)$. Parameter: x/s

travel at the body wave velocities α and β. In agreement with theory (Haskell, 1969; Richards, 1976) the starting signal P, which is found in the x-direction only in the near field, has the opposite sign as the final static displacement. On the component v the S-type stopping signals seem to be more prominent. On the curve $v(16 \cdot s, 0, t)$ a clear kink appears at the expected travel time of S_2 rather than of P_2 and R_2, whereas on the other curve $v(8 \cdot s, 0, t)$ the situation is not so clear because the expected arrival times are not well separated.

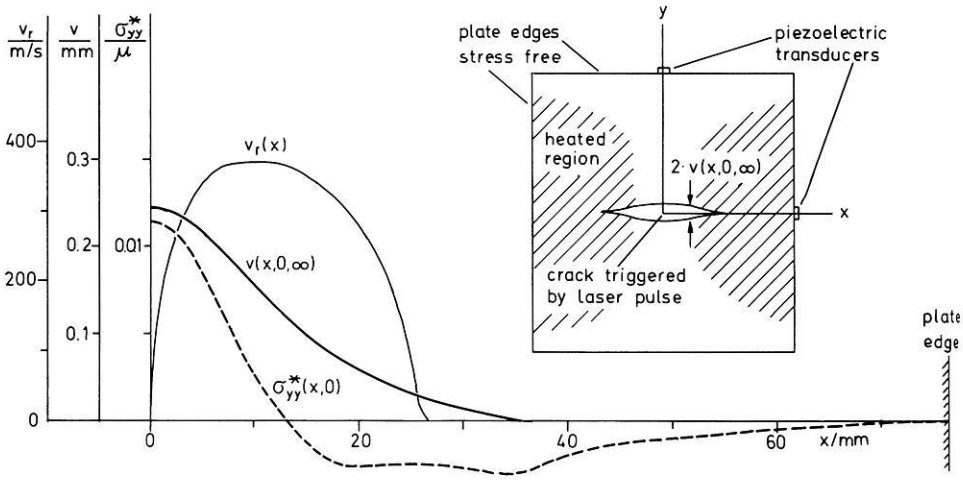

Fig. 10. Experimental data of tensile fracture experiments with Araldite B. $v_r(x)$: measured fracture velocity; $v(x, 0, \infty)$: crack separation measured after fracture; $\sigma^*_{yy}(x, 0)$: stress before fracture (calculated from $v(x, 0, \infty)$)

5. Simulation of Fracture Experiments

The prescribed constant fracture velocity of the standard models is, of course, not very realistic. Furthermore, in a homogeneous material a crack will stop only if the prestress is nonhomogeneous. The following experiments and their finite difference simulation were described by Auer and Berckhemer (1972), Auer (1974), and Stöckl and Auer (1976). Some of their ideas should be useful for realistic earthquake models, although the results are not directly applicable, since they correspond to mode I cracks. Plates of Araldite *B*, a homogeneous, isotropic, photoelastically sensitive material with the dimensions $16 \times 15 \times 0.3$ cm^3 were stretched in the y-direction (Fig. 10). Heating relieved the stress on the left and the right side. After cooling the plates were removed from the apparatus. The photoelastic pattern revealed remaining internal stresses, which were more or less symmetrical to the x- and y-axis.

Then a laser pulse was focussed into the centre of the plates. This triggered a crack, which propagated symmetrically in both directions along the x-axis, until the available elastic energy became too small. The crack interrupted thin strips of vapor sublimated aluminum, allowing the measurement of fracture velocity. At two points indicated in Figure 10 piezoelastic transducers recorded the acceleration. After fracture the separation of the crack surfaces, $2v(x, 0, \infty)$ was measured under a microscope.

Since some of the results were difficult to interpret, the experiments were simulated with the finite difference method. Suppose the crack is closed again. This requires an additional normal stress $\sigma^*_{yy}(x, 0)$ on the x-axis, which is equal to the prestress $\sigma_{yy}(x, 0, 0)$ on the crack surface. In the finite difference simulation the measured final crack surface displacement $v(x, 0, \infty)$ is applied in-

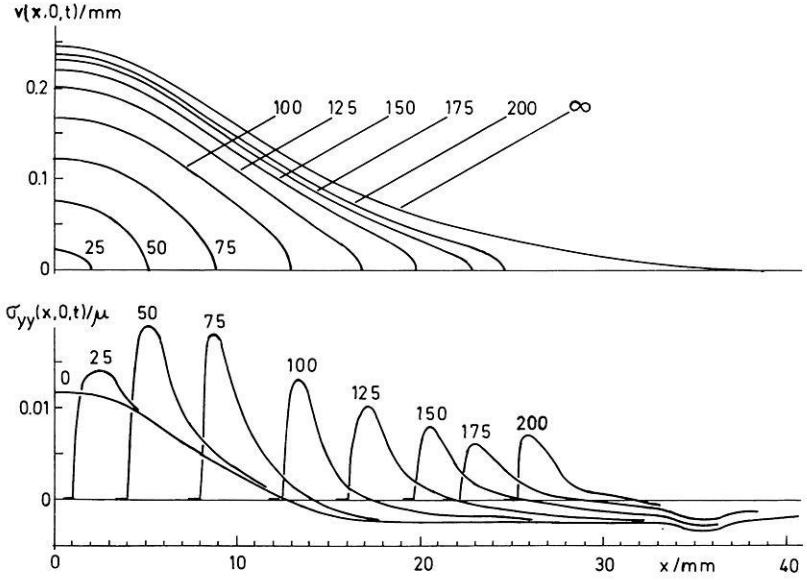

Fig. 11. Numerical simulation of tensile fracture experiments with Araldite B. Above: crack separation $v(x,0,t)$. Below: stress ahead of the crack tip $\sigma_{yy}(x,0,t)/\mu$ (tensile stress positive). Parameter: time step n ($\Delta t = 0.46 \times 10^{-6}$ s)

stantaneously with a negative sign. A damping term is added to the left side of Equation (7), for example $(\partial u/\partial t)/T$, where T is a time constant. Physically, this term simulates a thin layer of a viscous fluid, which separates the elastic plates from a rigid block. It damps the vibrations until the static solution remains, from which the stress $\sigma^*_{yy}(x,0)$ is calculated (Fig. 10). An appropriate value of T is chosen which minimizes the computing time.

After this calculation the closed crack was released again at the measured fracture velocity and the associated dynamic displacement was calculated with the method of Section 3. The model satisfactority simulated the wave form and the amplitudes of the accelerogrammes, which exceeded 10^7 cm/s^2 in some experiments.

Figure 11 shows the simulated displacement of the crack surfaces. The point $x=y=0$ reached a maximum velocity of 4.8 m/s. The crack exceeds the range where the prestress is tensile (σ^*_{yy} positive in Fig. 11). At the instantaneous crack tip $\sigma_{yy}(x,0,t)$ is, however, always tensile.

The simulation of the experiments yielded the following approximate relation between v_r and the stress intensity factor K_I, which determines the strength of the stress singularity at the crack tip (the definition of K_I is $K_I = \lim_{x \to L} \sigma_{yy}(x,0)\,[2\pi(x-L)]^{\frac{1}{2}}$): v_r becomes greater 0 at a critical value $K_I = 30\ \mathrm{N\,mm^{-3/2}}$, reaches 250–300 m/s at $K_I = 50\ \mathrm{N\,mm^{-3/2}}$ and increases then linearly to 500–550 m/s at $K_I = 200$–$250\ \mathrm{N\,mm^{-3/2}}$. Crack branching inhibits larger values of v_r and K_I.

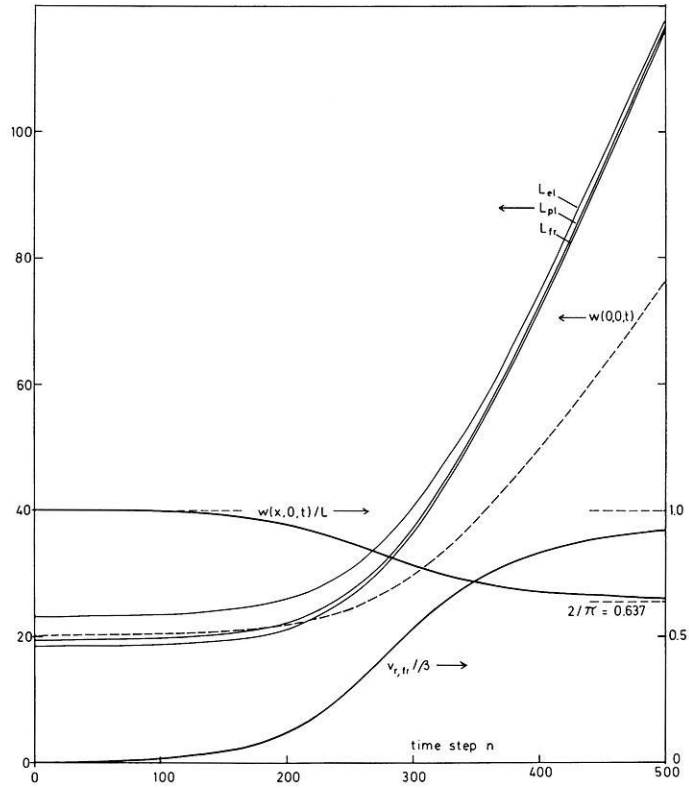

Fig. 12. Propagation of a mode-III-crack with constant fracture energy. Crack lengths L_{el}, L_{pl}, L_{fr} (unit: $\sqrt{2}s$), fracture velocity $v_{r,fr}=dl_{fr}/dt$, displacement at crack centre $w(0,0,t)$ (unit: $\sqrt{2}s\tau^0_{yz}/\mu$) as a function of time

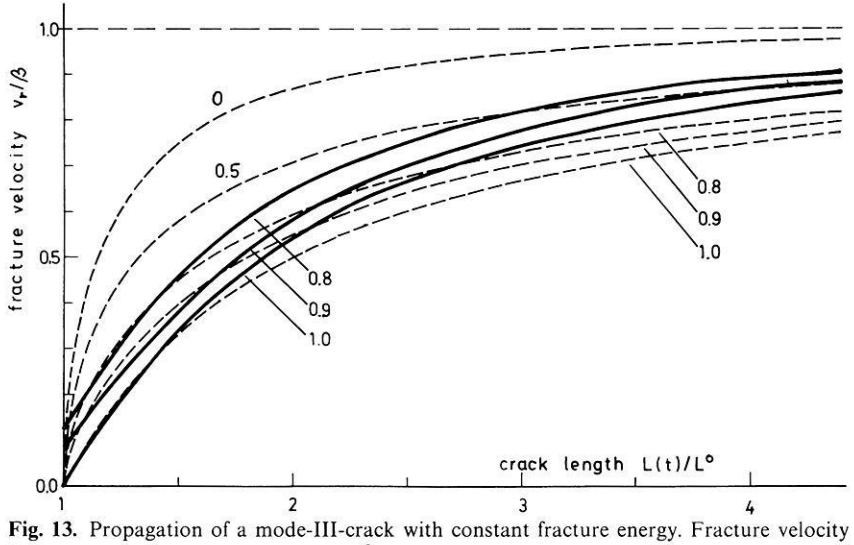

Fig. 13. Propagation of a mode-III-crack with constant fracture energy. Fracture velocity v_r/β as a function of crack length. Parameter: k^2. ———— finite difference solution; — — — — quasistatic theory

6. Crack Propagation at Constant Fracture Energy

Crack propagation is governed by the energy balance equation

$$dA/dt = dE_{el}/dt + dE_{kin}/dt + dE_d/dt. \tag{18}$$

A is the work done by the applied forces, E_{el} is the elastic energy, E_{kin} is the kinetic energy. The dissipated energy E_d is proportional to the specific fracture energy γ_F.

Let us consider a static mode III-crack. Following Griffith, one finds that the crack will grow, if

$$k^2 \equiv 4\mu\gamma_F/\pi L^0 \tau_{yz}^{02} \leqq 1, \tag{19}$$

where $2L^0$ is the initial length of a crack parallel to the x-axis, τ_{yz}^0 is the homogeneous prestress. Assuming that the dynamic displacement field is similar to the static field with the same length, one can estimate E_{kin} and obtains from Equation (18) (Erdogan, 1968):

$$v_r^2 = v_T^2(1 - L^0/L)(1 - (2 \cdot k^2 - 1)\, L^0/L). \tag{20}$$

This quasistatic approach, which is originally due to Mott, is elastodynamically not quite correct. It does not predict the correct terminal fracture velocity v_T for $L \to \infty$, which is equal to β according to analysis. This problem of an accelerating crack is probably too difficult for an exact analytic solution. Therefore, a finite difference solution, the details of which are found in Stöckl (1976), is outlined here.

The fracture energy is dissipated in a thin strip ahead of the crack tip, which deforms plastically. In this strip the stress increases linearly with strain up to an elastic limit, then remains constant up to a plastic limit and finally decreases and becomes zero at a third limit where new free surface is generated. This stress-strain relationship can be simulated in the boundary conditions. The grid is arranged as shown in Figure 2c. L^0, τ_{yz}^0 and γ_F are chosen such that the crack is just on the threshold of stability according to Equation (19). First, the static solution is found with a similar method as described in Section 5. Then γ_F is slightly lowered. Figure 12 shows how the crack becomes unstable, accelerates and finally attains the constant terminal velocity $v_T = \beta$. The three crack lengths L_{el}, L_{pl}, L_{fr} refer to the places where the three limits of elasticity, plasticity and generation of free surface are exceeded. L is an equivalent crack length corresponding to the case of negligible plastic zone size and is approximately equal to the average of L_{el}, L_{pl}, L_{fr}. $w(x, 0, t)$ is still almost exactly elliptical, but the aspect ratio $w(x, 0, t)/L(t)$ decreases with time.

Figure 13 shows the fracture velocity as a function of the crack length. The continuous lines represent the finite difference solution, which is supposed to be correct within the accuracy of the method. The dashed lines are calculated from Equation (20), where $v_T = \beta$ was taken. The deviation is significant, but Equation (20) may be regarded as a fair approximation.

7. Discussion and Conclusions

Despite the obvious advantages of stress relaxation models, dislocation models are still very useful. Having looked at the results of stress relaxation models, one may be able to construct more realistic dislocation models. The farfield displacement cannot be calculated with the finite difference method, since this would require too much storage and computing time. Therefore, I used the solution on the fault plane to obtain the farfield solution with a dislocation model.

For the standard models, some essential features of the near field were also found in a modified form in the far field. The stopping signals appear as clear kinks. Corresponding to the overshoot over the static value the time function falls below the zero line in the far field. This causes a small maximum in the spectral amplitude curve near the corner frequency. At high frequencies the amplitude spectra decrease as ω^{-2}, since there are discontinuities in the first time derivative. The dynamic overshoot could occur in deep focus earthquakes, if a low viscosity melt lubricates the fault planes. In shallow earthquakes friction will probably prevent an overshoot. If the fracture decelerates before stopping or if the prestress decreases towards the crack end, the stopping signals are smeared out and no longer recognizeable.

Although it takes more sophisticated models to explain measured near field accelerogrammes, the standard models allow the estimation of maximum velocity and acceleration. For example, model SIII scaled to a fault length of $2L = 10\,\text{km}$, a stress drop of 30 bars, $v_r = \beta = 3\,\text{km/s}$ yields an acceleration of about $5\,\text{m/s}^2$ and a velocity of 0.3 m/s in a distance of 7 km from the hypocentre in the frequency range 5–10 Hz, which seems quite realistic. To obtain this result with a dislocation model, one must assume an additional quantity, for instance the rise time of a ramp function.

In order to understand why an earthquake rupture arrests, one must probably consider nonhomogeneous prestress fields. Section 5 gives an idea how such problems can be treated with a finite difference method. Once the relation between v_r and the stress intensity factor K is found experimentally, the computer programme can calculate v_r from the instantaneous value of K. With respect to earthquakes, we are far from this goal. In the meantime, one may theoretically postulate some fracture criteria as demonstrated in Section 6. The fracture energy γ_F may depend on v_r or on the size of the crack. If v_r is to reach a terminal velocity $v_T < \beta$ in a mode III crack, γ_F must increase strongly as v_r approaches v_T, or it must increase linearly with L. For mode I and mode II cracks β must be replaced by v_R, as it turns out.

Although some stress relaxation problems have been solved analytically, realistic earthquake sources are probably too difficult for analysis. The finite difference method of Alterman and co-workers proved very successful in the numerical solution. It is straight forward, easy to use and to program. The standard model SII takes only about 60 FORTRAN statements, and 250 time steps for an array of 110×110 grid points are calculated in 3.5 min on an UNIVAC 1108 computer.

Whenever the results of the finite difference method of analytic calculations could be compared, they agreed satisfactorily. For instance, the maximum error,

which occurs near the crack tip, is about 1 % of the displacement at the middle of the crack for $L = 15 \cdot s$. Equation (17) could be verified with an accuracy better than 0.1 %.

Of course, the method has also some limitations. For instance, suppose that the propagation of a step function is simulated with Equation (9). One observes that the time function increases gradually before the theoretical arrival of the step and oscillates afterwards. These oscillations can be filtered out, but some loss of high frequency resolution cannot be avoided. This effect depends on the direction of propagation: For instance, Equation (9b) simulates waves propagating in the direction of the mesh diagonal without any distortion. In some applications it is therefore advantageous to choose the arrangement of Figure 2c, which was done in Section 4.1 and 6. This results in very sharp stopping signals. With the appropriate caution these limitations are not very serious.

Acknowledgments. The research work of this contribution was mainly done at the Institut für Meteorologie und Geophysik der Universität Frankfurt under the guidance of Prof. Dr. H. Berckhemer. The Deutsche Forschungsgemeinschaft supported it under contract nos. Be 299/31 and Be 299/34.

References

Alterman, Z., Burridge, R., Loewenthal, D.: The vibration of an elastic plane and half plane due to the sudden appearance of a crack. Geophys. J. **25**, 239–259, 1971

Alterman, Z.S., Loewenthal, D.: Seismic waves in a quarter and threequarter plane. Geophys. J. **20**, 101–121, 1970

Alterman, Z.S., Rotenberg, A.: Seismic waves in a quarter plane. Bull. Seism. Soc. Am. **59**, 347–368, 1969

Andrews, D.J.: Rupture velocity of plane shear cracks. J. Geophys. Res. **81**, 5679–5687, 1976

Archambeau, C.B.: General theory of elastodynamic source fields. Rev. Geophys. **6**, 241–288, 1968

Auer, F.: Getriggerte Bruchvorgänge als Modell für die Entstehung von Tieferdbeben. Diss. Frankfurt, 1974

Auer, F., Berckhemer, H.: Deep focus earthquakes as triggered dislocation processes. Phys. Earth Planet. Interiors **6**, 300–305, 1972

Burridge, R., Knopoff, L.: Body force equivalents for seismic dislocations. Bull. Seism. Soc. Am. **54**, 1875–1888, 1964

Erdogan, F.: Crack propagation theories. In: Fracture (H. Liebowitz, ed.), Vol. II. New York-London: Academic Press 1968

Haskell, N.A.: Elastic displacements in the near-field of a propagating fault. Bull. Seism. Soc. Am. **54**, 369–376, 1969

Ilan, A., Ungar, A., Alterman, Z.: An improved representation of boundary conditions in finite difference schemes for seismological problems. Geophys. J. **43**, 727–745, 1975

Madariaga, R.: Dynamics of an expanding circular fault, Bull. Seism. Soc. Am. **66**, 639–666, 1976

Richards, P.: Dynamic motions near an earthquake fault: A threedimensional solution. Bull. Seism. Soc. Am. **66**, 1–32, 1976

Stöckl, H.: Die Berechnung des dynamischen Bewegungsablaufs im Erdbebenherd. Diss. Frankfurt, 1976

Stöckl, H., Auer, F.: Dynamic behaviour of a tensile crack: finite difference simulation of fracture experiments. Int. J. Fract. **12**, 345–358, 1976

Received December 12, 1976; Revised Version January 31, 1977